

Chapter 1

The Large Hadron Collider and the ATLAS Detector

The Large Hadron Collider (LHC) [1–4] is a synchrotron collider located at the Conseil Européen pour la Recherche Nucléaire (CERN) near Geneva, Switzerland. It is also the world’s most powerful particle accelerator, providing both proton-proton (pp) and heavy ion collisions at the high energy frontier. At maximum speed, the protons in the LHC are only 3 m s^{-1} slower than the speed of light.

Four primary experiments utilize the TeV scale collisions generated at each of the four interaction points (IPs) of the LHC. Two general-purpose experiments, ATLAS [5] and CMS [6], employ hermetic detectors to study various physics processes. The LHCb experiment [7] focuses on measuring the properties of B mesons and other particles containing b-quarks, which are significant for understanding CP violation. The Alice experiment [8] investigates the properties of quark-gluon plasma, a state of matter believed to have existed in the early universe. Additionally, the LHC hosts several smaller, highly specialized experiments including LHCf [9], TOTEM [10], MoEDAL [11], FASER [12], and SND@LHC [13]. All LHC experiments strive to answer fundamental questions about the universe; to test the predictions of the Standard Model of particle physics or to search for new physics beyond it.

This section describes common collider physics definitions, such as the coordinate system and luminosity, the LHC along with its injector chain, and the ATLAS experiment. As the focus of this work is on data and tools for pp collisions at the LHC, the discussion is limited to this context. Additionally, the components of this thesis which utilized official ATLAS simulation and software, ??, were limited to tracks and jets. Therefore, the information provided here is focused on these topics only.

1.1 The Large Hadron Collider

The LHC is a somewhat circular collider with a circumference of 26.7 km. It is closer to an irregular octagon with rounded corners and approximately 530 **m** long straight sections, housed within a tunnel whose depth varies between 45 **m** and 170 **m** underground.

The machine consists of two ring acceleration pipes, each carrying a separate beam of protons or heavy ions that are accelerated in opposite directions. The beams are surrounded by 1232 superconducting niobium-titanium (NbTi) dipole magnets that generate an 8.33 T magnetic field to bend the protons around the curved sections

of the ring. Many more higher-order multipole magnets are used for beam insertion, cleaning, dumping, and focusing towards the experiment IPs. Along one of the straight sections, 16 superconducting radiofrequency cavities, eight per beam, operate at 400 MHz to accelerate the protons to their maximum energy. The LHC was designed to deliver a centre-of-mass energy of $\sqrt{s} = 14$ TeV but has yet to reach this due to technical limitations.

The beams are not continuous streams of protons but are instead segmented into bunches, each containing on the order of 10^{11} particles. The radiofrequency cavities are tuned to ensure that these bunches are tightly packed, each as long as 7.5 cm and separated by only 25 ns. For collisions to occur, the bunches from the two opposing beams are compressed to a space of 64 μm , around the width of a strand of hair, and made to pass through each other. Even with such compression and more than a hundred billion protons in each bunch, the average number of interactions per bunch crossing $\langle \mu \rangle$ is less than 100.

1.1.1 The CERN Accelerator Complex

The LHC is a synchrotron, meaning that it cannot accelerate particles from rest. Therefore, it is only the final stage of the CERN accelerator complex, which is shown in Figure 1.1. Each stage in the chain of accelerators increases the energy of the particles within before passing them to the next stage. Before 2020, the chain began with the Linear Accelerator (Linac) 2, which accelerated protons to 50 MeV. The input to Linac2 was hydrogen gas, stripped of its electrons by a strong electric field. Following Run 2, the chain was updated to begin with Linac4, which operates on negative hydrogen ions, not protons. This change reduces the beam loss, allowing more particles to accumulate in the next stage. Furthermore, Linac4 introduce a three-fold increase in beam energy, outputting particles at 160 MeV. The Linacs feed the Proton Synchrotron Booster (PSB), which increases the energy to 2 GeV and also serves to strip the electrons from the hydrogen ions. From the PSB, the protons are passed to the Proton Synchrotron (PS), which accelerates them to 26 GeV, and then to the Super Proton Synchrotron (SPS), which accelerates them to 450 GeV. From there, they are injected into the LHC. This entire process takes a few seconds, but several minutes are required to fill the entire bunch train of the LHC. The LHC then accelerates the bunches to the final energy, which, as of Run 3, is 6.8 TeV per beam.

1.1.2 Coordinate Systems

In collider experiments, the typical coordinate system places the origin at the nominal IP, which, for hermetic detectors like ATLAS, Alice, and CMS, is at the centre of the detector. The coordinate systems used by these experiments are right-handed, as shown in Figure 1.2, with the z -axis points along the beamline, the y -axis pointing upwards, and the x -axis pointing towards the centre of the LHC ring. The transverse plane is defined as the plane perpendicular to the beam axis and is spanned by the x and y coordinates.

A polar representation is also often used, where the azimuthal angle ϕ is measured in the transverse plane from the x -axis, and the polar angle θ is measured from the z -axis. The polar angle is frequently replaced with pseudorapidity η , defined as

$$\eta = -\ln \left(\tan \left(\frac{\theta}{2} \right) \right). \quad (1.1)$$

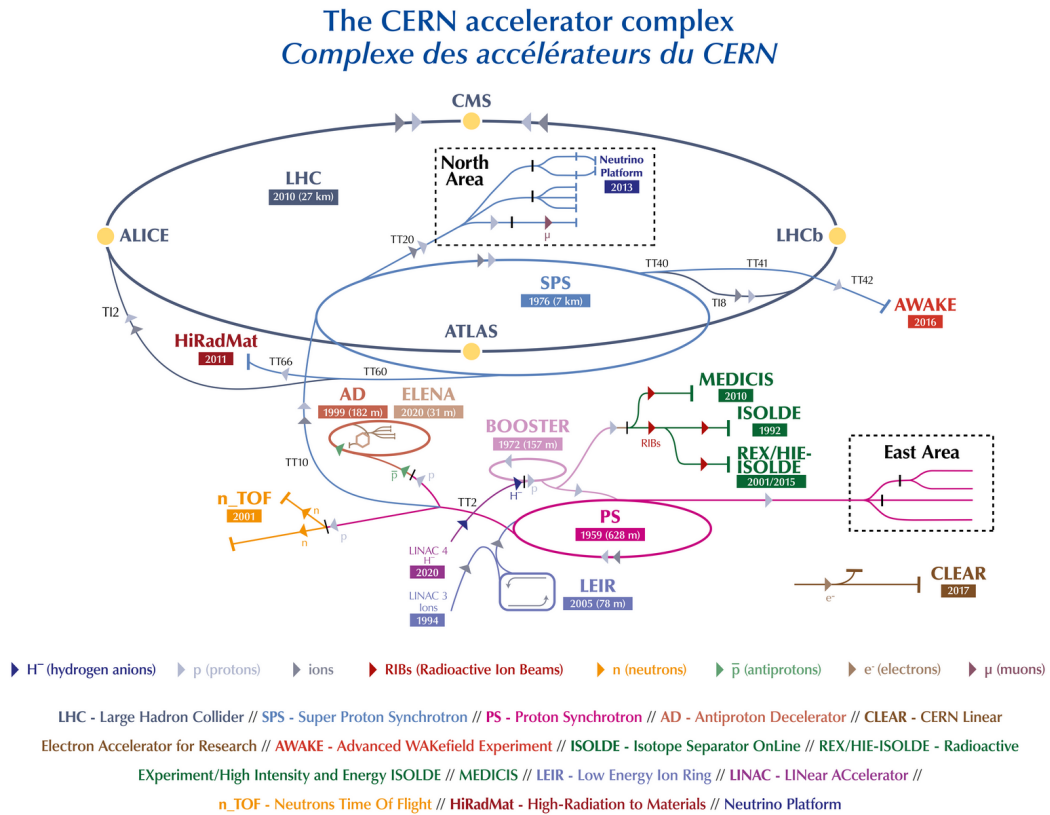


FIGURE 1.1: The layout of the CERN accelerator complex as of 2022 [14].

Differences in pseudorapidity are Lorentz invariant under boosts in the direction of the beamline, making it a useful quantity for describing the products of high-energy collisions.

Angular distances between objects are often measured in $\Delta R = \sqrt{(\Delta\eta)^2 + (\Delta\phi)^2}$, where $\Delta\eta$ and $\Delta\phi$ are the differences in pseudorapidity and azimuthal angle. For collision products, a key observable is a transverse momentum $p_T = \sqrt{p_x^2 + p_y^2}$, where p_x and p_y are the components of the momentum in the transverse plane.

1.1.3 Cross-Section and Luminosity

The cross-section, denoted by σ , indicates the likelihood of an interaction between two colliding particles. Although calculating the cross-section involves quantum

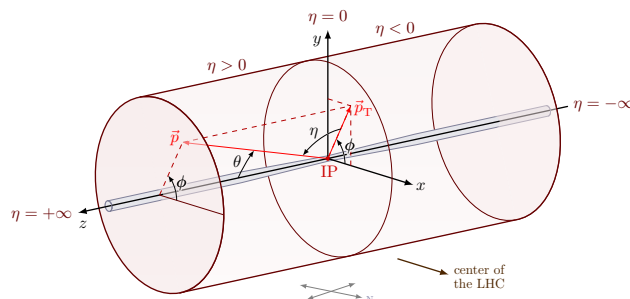


FIGURE 1.2: The right-handed coordinate system used by the ATLAS experiment.

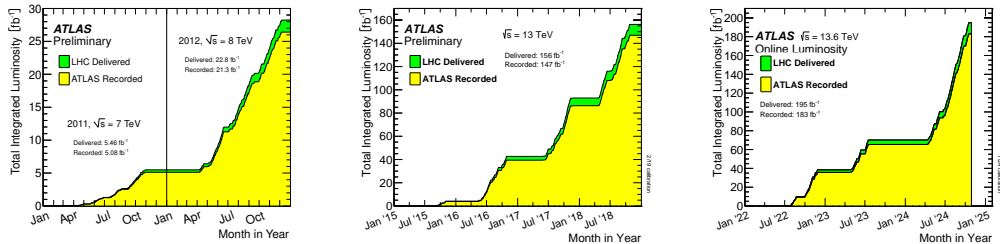


FIGURE 1.3: The total integrated luminosity delivered by the LHC and recorded by the ATLAS experiment for Run 1 (left) [15], Run 2 (middle) [16], and Run 3 (right) [17].

mechanical transition matrix elements and phase space integrals, it can be likened to the effective cross-sectional area of the particles participating in the interaction.

The total number of interactions N depends on the cross-section of the process σ and the integrated luminosity L_{int} by the formula,

$$N = \sigma L_{\text{int}} = \sigma \int \mathcal{L}(t) dt, \quad (1.2)$$

where $\mathcal{L}(t)$ is the instantaneous luminosity. This measures how tightly packed colliding particles are in a unit of space and time. For two colliding beams with Gaussian densities, the instantaneous luminosity is given by

$$\mathcal{L}(t) = \frac{N_1 N_2 f}{4\pi\sigma_x\sigma_y} S(\theta_c), \quad (1.3)$$

where N_1 and N_2 are the number of particles in each beam, f is the frequency of bunch crossings, σ_x and σ_y are the root-mean-square beam widths in the x and y directions, and $S(\theta_c)$ is the geometric reduction factor due to the crossing angle θ_c . This last factor exists because the beams do not collide head-on, as this would result in multiple collision points, so they are crossed at a finite angle θ_c . This reduces the overlap of the beams when they pass through one another, reducing the effective luminosity. For the $p p$ collisions at the LHC $S(\theta_c)$ is approximately 0.61. Even with this finite angle, long-range beam-beam interactions can still occur and must be accounted for.

The LHC was designed to deliver $\mathcal{L}(t) = 10^{34} \text{ cm}^{-2}\text{s}^{-1}$ at the IPs of ATLAS and CMS. However, this has not been constant over the years, and each experiment independently measures the luminosity using well-understood processes. The total integrated luminosity delivered by the LHC and recorded by ATLAS is shown in Figure 1.3. The LHC's instantaneous luminosity has increased with each run and this is particularly beneficial for measurements on rare events where the uncertainty is statistically limited.

1.1.4 Pileup

The increase in luminosity between Run 1 and Run 3 was in part achieved by raising the number of protons per bunch. This in turn leads to more particle interactions per bunch crossing. One of the undesirable effects of this is the large amount of overlapping signals in the detector which can degrade the resolution and efficiency of reconstruction algorithms.

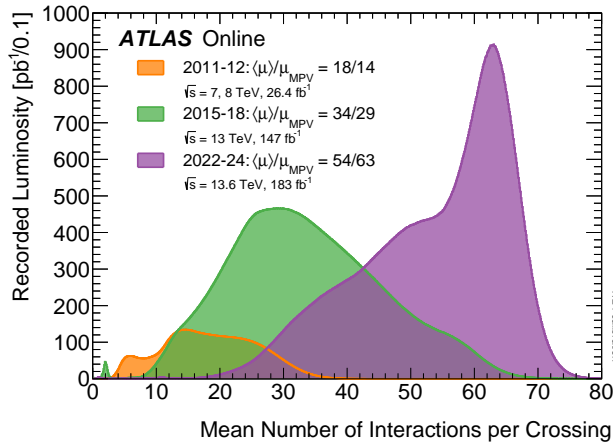


FIGURE 1.4: The distribution of the number of interactions per bunch crossing over the three LHC runs as measured by the ATLAS experiment [17].

Each bunch crossing in the collider generates a distinct event for analysis. While the average number of interactions per crossing has increased with each LHC run, Figure 1.4 shows a wide distribution of interaction counts within each run. Generally, only one of these interactions – the hard scatter – produces the high-energy particles captured by the detector and thus is of primary interest. The remaining “soft scatters” are low-energy interactions that are known as in-time pileup. Detector materials have a response and reset time, which can lead to residual signals from previous crossing being rerecorded, this is known as out-of-time pileup. Filtering out signals from all pileup sources is crucial for accurate data analysis and poses a significant challenge as the LHC’s luminosity increases.

1.1.5 LHC Runs

The LHC operates on multi-year runs, the first beginning in 2010. In between each run is a period of *long-shutdown*, allowing for maintenance and upgrades to both the accelerator and the experiments. The various run properties are shown in Table 1.1. Due to an electrical fault damaging many of the superconducting magnets in 2008, Run 1 was much delayed and operated at a reduced $\sqrt{s} = 7 \text{ TeV}$ using a sparse bunch structure, only colliding at 20 MHz. In 2012, the energy was increased to $\sqrt{s} = 8 \text{ TeV}$. The total delivered luminosity of the run was 28.4 fb^{-1} . Run 2 spanned from 2015 to 2018, with an increased energy of $\sqrt{s} = 13 \text{ TeV}$, a bunch crossing rate of 40 MHz, and a total integrated luminosity of 156 fb^{-1} . Run 3 began in 2022 and is expected to continue until 2026 and has already surpassed Run 2 with 195 fb^{-1} of data delivered [17].

TABLE 1.1: Overview of the different LHC runs [15–19]. Values for Run 3 are preliminary as data is still being collected.

	$\sqrt{s} [\text{TeV}]$	$\mathcal{L}_{\text{int}} [\text{fb}^{-1}]$	Protons per bunch	Bunch spacing [ns]	$\langle\mu\rangle$
Run 1 (2010-2011)	7	5.5	1.45×10^{11}	50	10
Run 1 (2012)	8	22.8	1.6×10^{11}	50	21
Run 2 (2015-2028)	13	156	1.25×10^{11}	25	34
Run 3 (2022-)	13.6	195	1.8×10^{11}	25	50

1.2 The ATLAS Experiment

The ATLAS experiment [5, 20] is one of the four primary experiments at the LHC. It is the largest particle detector of the four, weighing 7000 tonnes and measuring 44 m long and 25 m in diameter. It is a general-purpose detector designed to explore a wide range of physics phenomena. To achieve this, it has multiple sub-detectors designed to capture a broad range of outgoing products from the $p\bar{p}$ collisions. The ATLAS detector is shown in Figure 1.5.

The detector is hermetic, meaning it covers nearly the entire solid angle of 4π . It is arranged in concentric cylindrical-like layers around the IP. Each layer contains a barrel region, which wraps around the beamline, and end-cap regions, which cover the flat edges of the cylinder on either side.

This section describes the ATLAS detector, focusing on the tracking systems. These systems provide precise position and momentum measurements of charged particles, which are used to reconstruct particle trajectories and vertices.

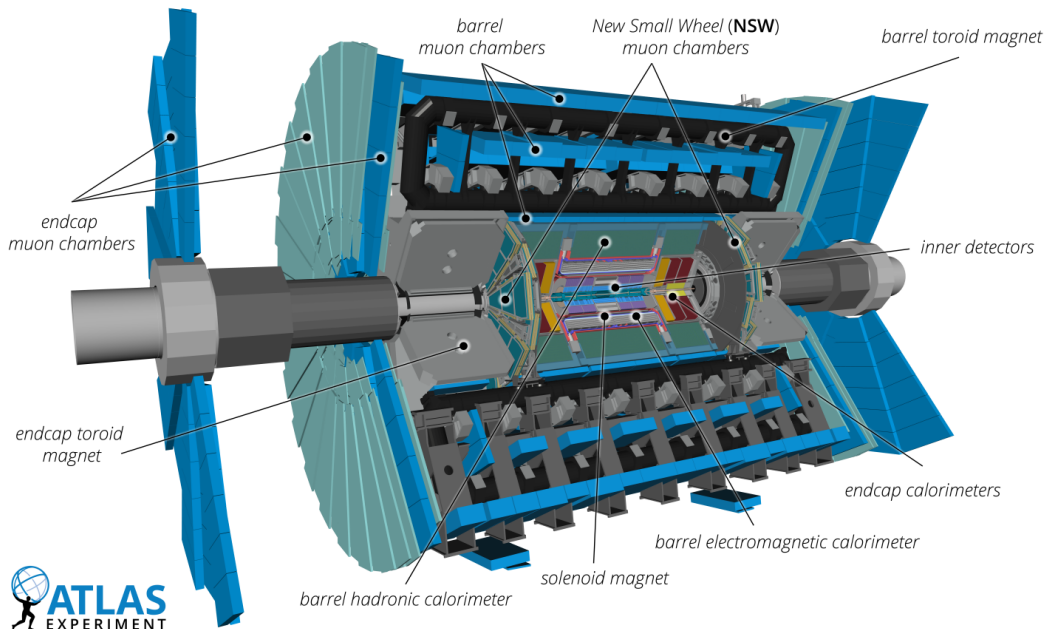


FIGURE 1.5: The ATLAS detector at the LHC. Image taken from Ref. [20].

1.2.1 Inner Detector

The Inner Detector (ID) is the innermost sub-detector of ATLAS and is shown in Figure 1.7. It comprises three sub-detectors: the Pixel Detector, the Semi-Conductor Tracker (SCT), and the Transition Radiation Tracker (TRT). It is designed to capture charged particle signals with a pseudorapidity $|\eta| < 2.5$. These signals are clustered into points in space where the particles have ionized the detector material. These points can be used to reconstruct the charged particle's trajectory – track – as it propagates out from the centre of the detector.

The ID is immersed in a 2 T axial magnetic field generated by a 5.8 m long superconducting solenoid magnet containing over 9km of NbTi wire. The magnetic field causes the particles to bend in a plane perpendicular to the beamline, tracing out

a helical path whose curvature is proportional to q/p , where q is the charge of the particle and p is the magnitude of its momentum.

A fully reconstructed track is characterized by five parameters, which are shown in Figure 1.6. These include the charge-to-momentum ratio q/p , the azimuthal angle ϕ , the polar angle θ . By tracing the track back to the beamline, the longitudinal z_0 and transverse d_0 impact parameters are determined at the point of closest approach to the IP. These impact parameters represent the distances measured in each respective direction. The relative p_T resolution of the ID is described as,

$$\sigma\left(\frac{1}{p_T}\right) = 0.36 \oplus \frac{13}{p_T \sin(\theta)} \text{ TeV} \quad (1.4)$$

where \oplus denotes a sum in quadrature.

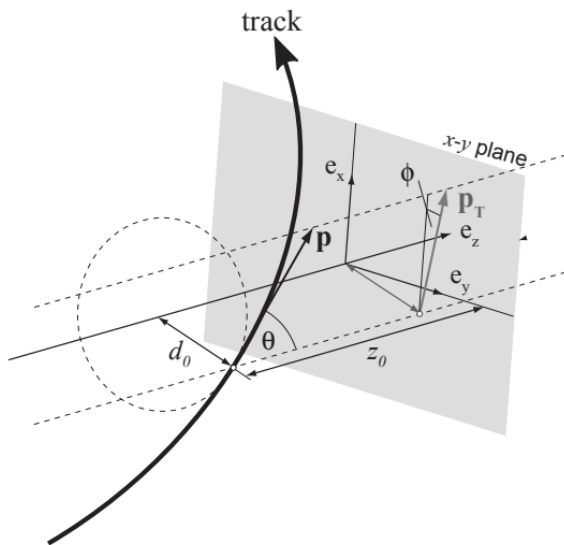


FIGURE 1.6: The main parameters of a reconstructed track in the ATLAS Inner Detector. Image taken from Ref. [21].

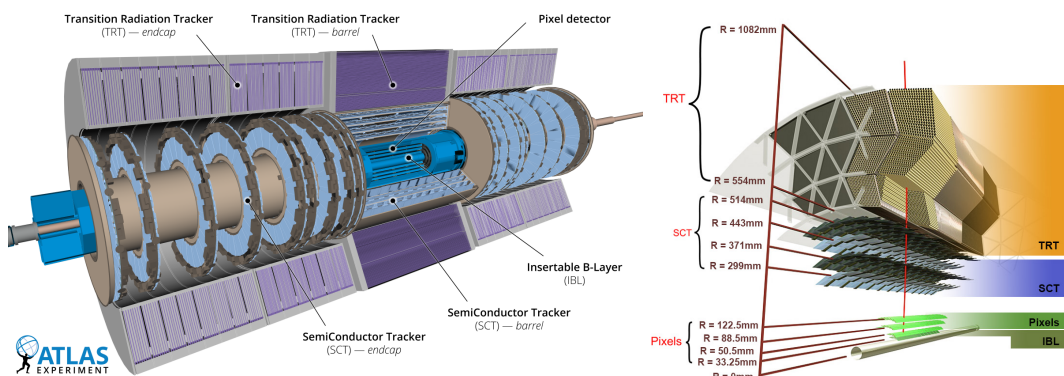


FIGURE 1.7: Schematic of the full ATLAS Inner Detector (left) and a cross-section of the barrel region (right). Images taken from Refs. [20, 22].

Pixel Detector

The high-granularity silicon pixel detector [23] covers the innermost region of the ID. It measures 1.4 m long and is fully contained in a diameter of 0.5 m. High granularity is required at this scale to resolve the numerous tracks that pass through it. Individual silicon pixels are about 50 μm wide in the transverse direction and about 400 μm long in the longitudinal direction.

Each pixel has a slight potential difference applied across it. Ionizing radiation left by a traversing charged particle generates electron-hole pairs that drift and are collected at the p-n junctions, providing a signal. The pixel detector has 1744 modules, each containing around 46k pixels, resulting in 80M readout channels. These are arranged in three barrel layers placed at a radius of 50.5 mm, 88.5 mm, and 122.5 mm from the beamline, with four end-cap disks on each side.

Between Run 1 and 2, an additional layer was added at a radius of 33 mm to the beamline, known as the Insertable B-Layer (IBL) [24]. Pixels in the IBL measure 50 μm in the transverse direction and 250 μm in the longitudinal direction. This layer improved the p_{T} resolution of the detector by close to 30% for low p_{T} tracks. Furthermore, the enhanced z-resolution improved impact parameter resolution and cluster separation, allowing for better reconstruction of primary and secondary vertices.

Semiconductor Tracker

The Semiconductor Tracker (SCT) [25] surrounds the Pixel Detector, occupying the region between 299 mm and 514 mm from the beamline. It comprises four concentric barrel layers with nine disks at each end-cap covering the region $|\eta| < 2.5$. Like the pixel detector, the SCT is composed of silicon readout channels. Unlike the pixels, each microstrip measures $20 \mu\text{m} \times 12 \text{ cm}$ and thus only has high granularity in a single direction, oriented to the transverse momentum. To improve longitudinal resolution, each SCT layer includes two back-to-back microstrip layers, rotated by 40mrad relative to each other. The SCT in total has around 6.3M readout channels.

TRT

The outermost sub-detector of the ID is the Transition Radiation Tracker (TRT) [26]. It is a straw-tube tracker that aids in the momentum measurement and provides information for particle identification for tracks within $|\eta| < 2.0$. The TRT provides the most hits per track, around 35 on average, of the three sub-detectors. At a greater distance from the beamline, it also does not require such fine spatial resolution as the silicon detectors to provide a good measurement of the track kinematics.

It comprises approximately 300k thin-walled drift tubes, each 4 mm in diameter. The barrel region contains 50k tubes, each 144 cm long, while the end caps contain 250k tubes, each 37 cm long. A potential difference exists between the tube walls and an axial wire. When a charged particle intersects the tube, it ionizes the predominantly argon gas inside, and the resulting electrons drift towards the wire, providing the signal. There is no information on where the ionization occurred along the length of the tube. Thus, resolution for the barrel region is only defined in the $r - \phi$ plane, and for the end-cap, it is only defined for $z - \phi$. A polymer foil is placed between the tubes to generate transition radiation, the pattern of which allows discriminating between electrons and pions.

1.2.2 Calorimeters

ATLAS has three calorimeter systems outside the central solenoid magnet, which measure the energies of particles produced by the collisions. Each calorimeter is designed with alternating layers of absorber and active materials. Particles interact with the absorbers, lose energy, and produce showers of secondary particles that ionize the active material, which can be converted into a measurable signal. These layers are typically arranged in an accordion-like structure to ensure homogenous coverage. Different absorber materials are used to optimize the interaction and thus containment of the showers for different particle types.

The Electromagnetic Calorimeter (ECal) is specialized for measuring the energies of electrons and photons. Surrounding this is the Hadronic Calorimeter (HCal), which is designed to measure the energies of hadrons. These subsystems cover the region $|\eta| < 3.2$. In addition, there is also the forward calorimeter subsystem, which measures the energy of particles in the range $3.2 < |\eta| < 4.9$. However, information from this subsystem is not used in this work, and it is omitted from the following descriptions. A schematic of the calorimeter systems is shown in Figure 1.8.

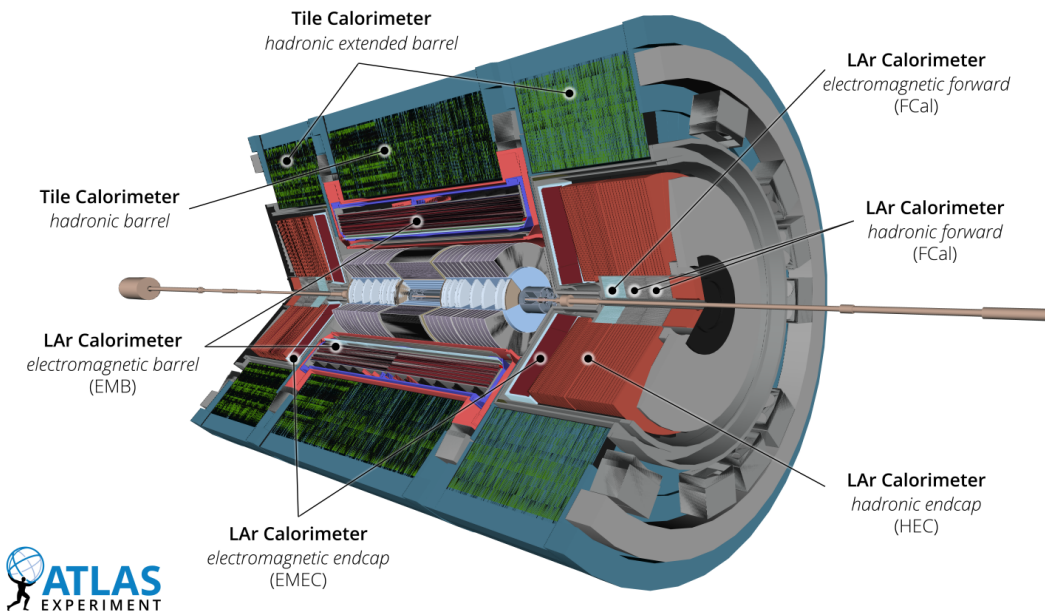


FIGURE 1.8: Schematic of the ATLAS calorimeter systems. Image taken from Ref. [20].

Electromagnetic Calorimeter

The Cal [27] is a high granularity calorimeter which uses liquid argon as the active material and lead as the absorber. To keep the argon in a liquid state, the ECal is cooled to -185°C . These materials are chosen to optimize the containment of electromagnetic showers produced by electrons and photons, via pair production and bremsstrahlung radiation, while minimising the energy loss of heavier particles. The barrel ECal covers the range $|\eta| < 1.475$ and is split into three layers, decreasing in granularity with distance from the beamline. The inner layer allows for more precise shower measurements which assists in the identification of pions. The Liquid

Argon Electromagnetic Enc-Cape (EMEC) and covers the range $1.375 < |\eta| < 3.2$. Unlike the ID, the ECal resolution increases with incident particle energy.

Hadronic Calorimeter

The HCal or Tile Calorimeter [28] encompasses the ECal and is designed to measure the energies of hadrons. It uses steel as the absorber and scintillating tiles as the active material made from polystyrene. The hadrons are contained by losing energy through inelastic nuclear interactions with the steel, producing a shower of electrons and photons which are detected by the tiles. In the forward regions of the calorimeter, $1.5 < |\eta| < 3.2$, a copper/LAr combination is used. The granularity and energy resolution of the HCal are lower than the ECal.

1.2.3 Muon Spectrometer

Other than neutrinos, which traverse the entire detector without interacting, muons are the only particles that easily penetrate through the calorimeters, incurring minimal energy loss. Though they leave tracks in the ID, the Muon Spectrometer (MS) [20, 29] provides triggering information, identification, and extra momentum measurements for muons. The MS is the outermost sub-detector of ATLAS and is shown in Figure 1.9. Its systems are arranged in three barrel layers covering $|\eta| < 1.2$ and several end-cap layers or wheels covering $1 < |\eta| < 2.7$. The wheels are placed on either side of the detector at a distance of 7.4 m, 14 m, and 21.5 m from the IP.

Monitored Drift Tubes are the spectrometer's primary tracking component and are similar in principle to the straw tubes in the TRT@. More than 380k aluminum tubes, each with a diameter of 30 mm and primarily filled with argon gas, are organized into three barrel layers and four end-cap disks. In addition, Cathode Strip Chambers are used in inner layers of the end-cap to cope with the higher particle flux. These are multi-wire proportional chambers built into strips.

Three large air-core toroidal magnets generate the magnetic field in the MS, one in the barrel region and one in each end-cap regions. Each magnet has eight coils and deflects the muons, allowing for the measurement of their momentum.

1.3 Reconstruction

Reconstruction is the process of converting the raw detector signals into collections of defined physical objects to better understand the collision events. This process is performed offline, after the data has been recorded and stored, and uses information from all sub-detectors.

This section describes the basics of track, vertex, and jet reconstruction at ATLAS, as well as several approaches to jet tagging.

1.3.1 Tracks

Track reconstruction refers to taking the collection of hits registered by the ID, and grouping them into individual tracks likely to have been produced by a single charged particle. Tracks are key ingredients in the reconstruction and identification of other particles, such as electrons and muons, jets, and the multiple vertices produced in each collision. A full description of the track reconstruction pipeline used for ATLAS

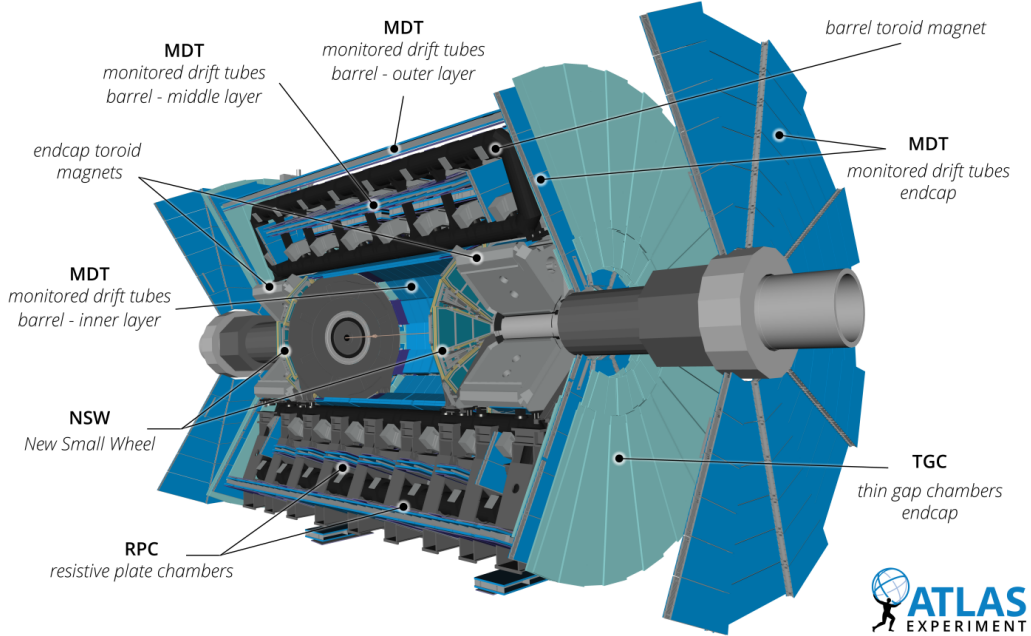


FIGURE 1.9: Schematic of the ATLAS Muon Spectrometer. Image taken from Ref. [20].

Run 2 data can be found in Ref. [30]. Track reconstruction is performed in numerous stages. Hits are first clustered into space points, after which iterative track-finding algorithms are used, followed by cleaning and ambiguity resolution.

Clusterization

A single particle may deposit energy in multiple adjacent pixels or strips in the ID. This is due to the drift of electrons between sensors within the solenoid magnetic field or from the incident angle of the particle. These hits are first combined into clusters which are then used to form *space points* (SP) defined in three dimensions. For the SCT, these clusters also combine information from the two back-to-back layers. Position uncertainties of these points are estimated from cluster sizes and detector geometry. In dense environments the clustering algorithm may merge mistakenly merge hits from different particles, leading to a higher rate of fake tracks.

Track Seeding

Tracks are *seeded* by grouping triplets of SPs in three sequential layers in either the pixel or SCT subdetectors. Each of these seeds forms a *track candidate* and are used to determine the first crude estimates of the track parameters, assuming a perfectly uniform magnetic field and helical trajectory. The only requirement to improve purity is that one additional SP is found compatible with the track candidate outside the seeding region.

A combinatorial Kalman filter [31] is employed to iteratively extend this candidate by incorporating additional SPs in the other layers both towards and away from the IP. If multiple compatible space-point extensions are found on the same layer, the filter generates several track candidates for each seed. At this stage, hits may be shared between multiple candidates, which is intentionally done to maximize the number of possible candidates and thus the efficiency of the algorithm.

The following steps are designed to improve the track quality and remove fake tracks.

Ambiguity Resolution

The ambiguity resolver begins by defining a *track score* for each candidate. This score quantifies the likelihood that each candidate corresponds to a real trajectory. The score takes into account several factors; the number of SP assigned to the track will increase its score, while the number of holes will decrease it. Holes are defined as intersections between the reconstructed track and active sensor material where no matching SP is found. They can be found in data due to inefficiencies in the silicon sensors. The track score also considers the χ^2 of the track fit. Tracks with higher p_T also receive a higher score. The ambiguity resolver then iterates over the list of track candidates in order of decreasing score.

Clusters can overlap naturally in high-density environments. These are referred to as *merged clusters*. A neural network estimates the number of particles traversing each cluster and their positions [32]. This information allows the cluster to be split and allocated to the different candidates. A track can have no more than two shared clusters, and clusters may be shared by no more than two tracks, with preference given to the track with the highest score. The refined and purified track candidates are then re-fit to obtain the final parameters. It obtains a new score and is inserted back into the list of candidates.

During this stage, seeds that fail the track-finding process are checked for compatibility with information from the calorimeter. If a seed is within a region of interest in the calorimeter, the track-finding procedure is repeated, permitting an extra *kink* in the track as this may have been caused by Bremsstrahlung radiation. This step improves electron reconstruction efficiency.

The ambiguity resolver fully rejects track candidates if they fail to meet the criteria in Table 1.2. If the track is processed twice by the resolver without modification, it is saved to the final collection and all associated hits are removed.

Parameter	Selection
p_T	$> 400 \text{ MeV}$
$ \eta $	< 2.5
$ d_0 $	$< 3.0 \text{ mm}$
$ z_0 \sin \theta $	$< 5 \text{ mm}$
Shared clusters	< 2
SCT + Pixel hits	≥ 8
Pixel holes	< 2
SCT + Pixel holes	< 3

TABLE 1.2: Track selection criteria used by the ambiguity resolver.

TRT Extension

Finally, information from the TRT is used to extend the tracks. A similar Kalman filter incorporates TRT hits starting from the predicted intersection between each silicon track and the TRT. If successful, the TRT hits are added to the track, and the whole track is fit once more using a global χ^2 fitter. The inclusion of TRT hits

enhances momentum resolution and allows for particle identification. However, the extension may be rejected if it worsens the χ^2 of the track candidate or if more than 50% of the TRT hits are tube hits with no leading edge.

1.3.2 Vertices

Vertex reconstruction is the process of identifying the many primary and secondary vertices produced in each collision. Each vertex is a location in space, constructed from a convergence of fully reconstructed tracks, and indicates the point of origin for multiple charged particles.

Primary vertices are those produced by the many pp collisions during the bunch crossing. For Run 1 and 2, the primary vertices are reconstructed using the Iterative Vertex Fitter [33]. First, a seed position of the vertex is selected using the mode of the z-coordinate all tracks in the event measured at the point of closest approach to the beamline. Next, the vertex position is iteratively refined, and in each iteration, less compatible tracks are down-weighted. After the final iteration, all tracks with low enough weights are removed from the vertex and used for the next.

For each event, the primary vertex with the highest $\sum p_T^2$ of all associated tracks is labelled as the *hard scatter vertex*. It is sometimes ambiguously referred to as *the* primary vertex (PV) while the others are referred to as *pileup* vertices. Reconstruction on Run 3 data is switching to an Adaptive Multi-Vertex Fitter [34].

Secondary vertices are those produced by the decay of particles originating from the PV. This secondary decay must take place at a distance sufficiently far away in the transverse plane to be resolved and not mistakenly identified as pileup. They are typically caused by the decay of long-lived b -hadrons or the interaction of particles with the detector material and are thus crucial tools for identifying b -jets. In ATLAS, secondary vertex reconstruction is performed within the context of jet reconstruction using the JetFitter [35] or SV1 [36] algorithms.

1.3.3 Jets

As described in ?? are an emergent property of QCD, which results in a collimated spray of particles stemming from the decay and fragmentation of an initiating color-charged parton. From a detector perspective, jets result in large localized energy deposits in both calorimeters and many tightly packed tracks in a cone emanating from the PV. The width of the jet cone is dependent on the mass of the initiating particle and its transverse momentum, with $\Delta R \approx 2m/p_T$.

Due to the stochastic nature of the showering process, the jet signal can never be perfectly isolated. Particles within the jet cone may overlap with other initial state radiation, multiple parton interactions (from the underlying event), or pileup. Jet reconstruction is, therefore, a difficult optimization problem. The goal is to maximally capture the energy of the initiating particle while minimizing the contamination from other sources. A jet reconstruction algorithm should capture all hard partons in the event, have an axis parallel to the jet momentum, and accept roughly uniform contamination.

Jet reconstruction in ATLAS is performed using the anti- k_t algorithm [37]. This is a sequential recombination algorithm that iteratively clusters a collection of objects. It is both infrared and collinear safe. The algorithm is defined by a maximum distance

parameter R . The algorithm begins with the hardest, highest p_{T} , object in the event i . During each iteration, the distance d_{ij} is calculated to all other objects j in the event,

$$d_{ij} = \frac{1}{\max(p_{\text{T}i}^2, p_{\text{T}j}^2)} \frac{\Delta R_{ij}^2}{R^2}. \quad (1.5)$$

If this value is less than $1/p_{\text{T}i}^2$, then the objects are combined, and the algorithm proceeds; otherwise, i is considered a jet and removed from the list. The algorithm continues until all objects are clustered or declared as jets.

Jets can be clustered using the anti- k_t algorithm with a variety of inputs. During Run 1, jets were constructed from topo-clusters, topologically connected calorimeter cells [38]. In some analyses, jets are clustered from tracks only [39]. The general approach for Run 2 and 3 data is to include both sets of information using the Particle Flow (PFlow) algorithm [40].

Particle Flow

The PFlow algorithm is designed to prevent the double-counting of momentum contributions from charged particles that leave both ID tracks and calorimeter energy deposits. This algorithm iterates through the tracks in descending p_{T} order, constructing charged PFlow objects. The algorithm begins by attempting to match the selected track to a topo-cluster in the calorimeter. Both are then used to compute the expected energy contribution to the cluster by the particle that created the track. A single particle may deposit energy in multiple topo-clusters, and the algorithm evaluates the probability of this occurring and may include additional topo-clusters if necessary. The expected energy is then subtracted from the associated topo-clusters, cell-by-cell. A new track is then selected, and the process is repeated. If, at any point, the remaining cell energy following the subtraction falls below expected shower fluctuations, it is removed.

Topo-clusters not matched to any tracks are deemed to have been produced from neutral particles and left unmodified. These, and the remaining clusters after the subtraction step, are used to construct neutral PFlow objects.

The output of the PFlow algorithm is a collection of charged and neutral PFlow objects, each with defined energy and momentum. Charged PFlow objects not matched to the PV are removed to reduce pileup contamination. The remaining objects are clustered into jets using the anti- k_t algorithm with $R = 0.4$.

Jet Association

Once jets are defined, other objects can be associated using a ΔR matching criterion. For instance, a jet might be constructed from calorimeter energy deposits, but tracks can still be associated. The width of the ΔR association cone typically decreases as with jet p_{T} . This track association is beneficial for the ATLAS experiment because it enables using the Jet Vertex Tagger (JVT) [41]. The JVT leverages the transverse momenta from associated tracks to discriminate against jets originating from pileup interactions. Furthermore, many of the flavour tagging algorithms mentioned in the next section and in Section 1.3.5 operate on the set of tracks associated with a jet, even though the jets themselves were clustered from PFlow objects.

1.3.4 Large Radius “Fat” Jets

Many decay channels of massive particles result in multiple parton final states. Some examples that are frequently encountered include $W/Z \rightarrow q\bar{q}$, $t \rightarrow Wb \rightarrow q\bar{q}b$, and $H \rightarrow VV \rightarrow q\bar{q}q\bar{q}$. If the initiating particle is produced at rest in the lab frame, the final state partons would be emitted back-to-back and likely be reconstructed as individual jets. However, as the transverse momentum of the initiating particle increases, the decay products become more collimated, as shown in Figure 1.10. In the highly boosted regime, the parton showers overlap in the detector and may be reconstructed as a single jet. To fully capture these composite jets, the anti- k_T algorithm is run with a larger radius parameter of $R = 1.0$. These jets are colloquially referred to as *fat* jets.

The overlapping showers lead to a distinct internal substructure within the jet, with regions of high energy density called *subjets* or *prongs*. The processes listed above, for example, would lead to 2-prong, 3-prong, and 4-prong jets, respectively. Jets from non-resonant QCD processes tend to have smooth energy distributions and no substructure (1-prong).

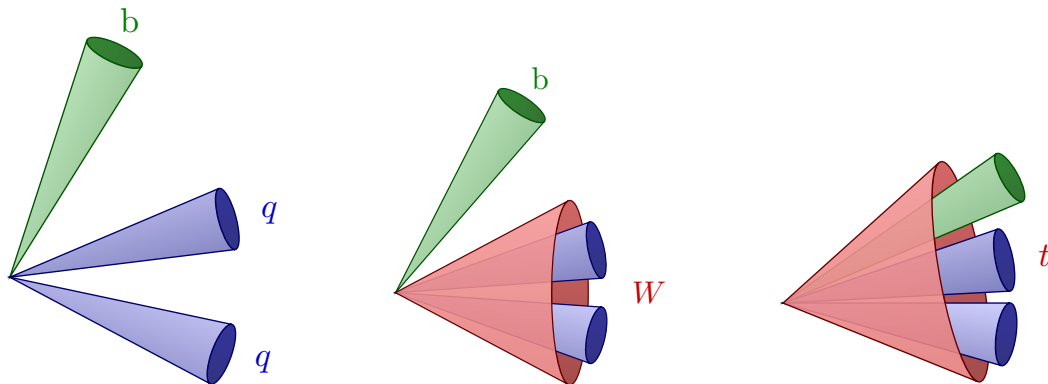


FIGURE 1.10: A top quark decay with increasing momentum, showing the transition from three separately resolved jets (left), to a W -jet and a b -jet (middle), to a single fat jet (right).

The number of subjets and the angular separation of these subjets can be used to identify the initiating particle. One commonly used set of observables to describe jet substructure is its *N-subjettiness* [42], denoted by τ_N . N-subjettiness is a measure of how well a jet can be decomposed into N subjets. For a given N these subjets can be found via some other clustering algorithm, such as the exclusive- k_t algorithm [43], and then the τ_N observable is defined as,

$$\tau_N = \frac{1}{p_T R} \sum_i \min(\Delta R_{1,i}, \Delta R_{2,i}, \dots, \Delta R_{N,i}), \quad (1.6)$$

where k runs over the constituents of the jet, and $\Delta R_{i,j}$ is the angular separation between the i th constituent and the j th subjet. The discriminating variable for jet tagging is often the ratio of these observables, $\tau_{21} = \tau_2/\tau_1$, is commonly used to distinguish vector boson jets from QCD jets, and $\tau_{32} = \tau_3/\tau_2$, is used to identify top quark jets.

Other commonly used observables relate to the jet’s energy correlation functions [44] and their ratios. Analyses at ATLAS make frequent use of the D_2 observable [45] to

separate 1-prong and 2-prong jets,

$$D_2 = \frac{e_3}{(e_2)^3}, \quad (1.7)$$

$$= \frac{\sum_{1 \leq i < j < k \leq N} z_i z_j z_k \Delta R_{ij} \Delta R_{ik} \Delta R_{jk}}{(\sum_{1 \leq i < j \leq N} z_i z_j \Delta R_{ij})^3}, \quad (1.8)$$

where z_i is the p_T fraction of the jet carried by the i th constituent, and ΔR_{ij} is the angular separation between the i th and j th constituents, and N is the number of constituents in the jet. Additionally, the Energy Flow Polynomials (EFPs) [46] are a set of basis features which are sensitive to the underlying substructure of different jet types.

1.3.5 Heavy-Flavour Tagging

Heavy-flavour tagging, or simply flavour tagging, is the process of identifying jets that contain the decay products of b -quarks (b -jets) or c -quarks (c -jets). Jets originating from the decay of u -, d -, s - quarks and gluons are collectively called light-jets. Identifying jets from either process is known as b -tagging or c -tagging, respectively. In ATLAS, b -tagging plays a critical role in many analyses, particularly those measuring properties of the Higgs boson or the top quark. Nearly all top quarks decay rapidly into a W -boson and a b -quark, and the dominant decay mode of the Higgs boson is to a pair of b -quarks.

Unlike the methods to distinguish large-radius jets, which rely on the jet substructure, the main distinguishing feature used in b -tagging is the extended lifetime of hadrons containing b -quarks. As discussed in ??, the weak interaction CKM matrix is nearly diagonal, thus favouring transitions within the same generation. However, the b -quark is approximately 40 times lighter than the t -quark; it can only decay into lighter generations and is thus CKM suppressed.

The b -hadrons are quasi-stable bound states between a b -quark and one or two lighter quarks. They have an average lifetime of around 1.5 ps, and if emitted with $p_T = 50$ GeV would travel around $L_{xy} = 5$ mm in the transverse plane before decaying. This distance can be resolved by the ID vertex fitting algorithms and would result in a vertex with a notable transverse displacement, as shown in Figure 1.11. The presence of a high mass secondary vertex within a jet is the primary feature used in b -tagging

Flavour tagging at ATLAS has evolved over many years. Typically, the tools return the likelihood of a b - c - or light-jet, given some properties of the associated tracks. A collection of comparisons between these algorithms used in b -tagging is shown in Figure 1.13. Several handcrafted algorithms were designed for flavour tagging before the start of Run 1, such as IPxD [48], SV1 [36], and JetFitter [35]. Each tagger used a unique approach to extract different high level features from the jet and associated tracks. They also yielded different performances depending on the phase space. It was found that combining the most discriminating features from each in a single neural network resulted in a more versatile tagger known as MV1 [49], which was used at the start of Run 1. At the start of Run 2, it was replaced by MV2 [50], a boosted decision tree with similar inputs. In 2017, it was replaced by DL1 [51], a neural network again with much the same approach. These figures plot the b -jet efficiency against light and c -jet rejection.

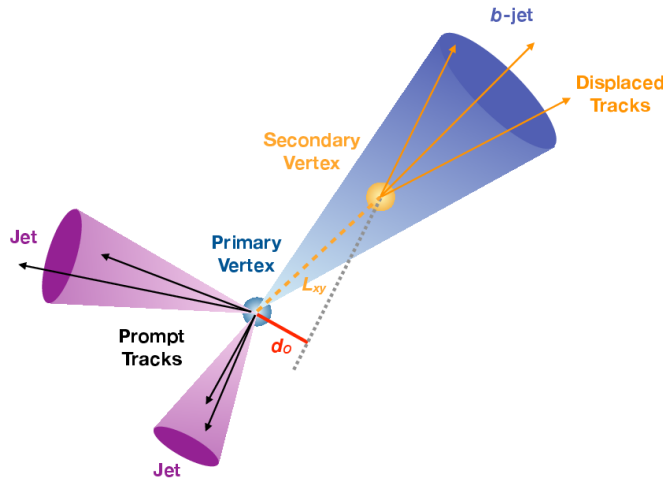


FIGURE 1.11: An interaction producing two light-flavour jets and one b -jet in the transverse plane. B -hadrons have a transverse decay length L_{xy} of a few millimetres, creating displaced tracks and a secondary vertex. The transverse impact parameter (d_0) is the closest approach distance of these tracks to the primary vertex, typically large for b -hadrons. Image taken from Ref. [47].

Also introduced at this time was the first tagger based purely on the raw collection of tracks and their parameters, known as RNNIP [52]. This was a recurrent neural network (RNN) that processed all the tracks in the jet sequentially to determine the three class probabilities. Again, the performance could be improved by combining the outputs of RNNIP with the other IPxD, SV1, JetFitter. This combination yielded the DL1r tagger [53]. A second track-based tagger known as DIPS [54] was developed in 2020. It used the deep sets architecture [55], and the corresponding combined tagger was labelled DL1d [56].

The most recent iteration is a departure from the previous approach of combining multiple high level and track based taggers. In 2022 ATLAS introduced the GN1 tagger [57] which is a graph neural network, ??, that only uses the track information. This single network, as shown in Figure 1.12, simultaneously performs jet tagging, as well as vertex matching and track classification trained end-to-end.

More details on the GN1 tagger are provided in ??, which also details the development of a new flavour tagging algorithm, GN2, which would supersede it.

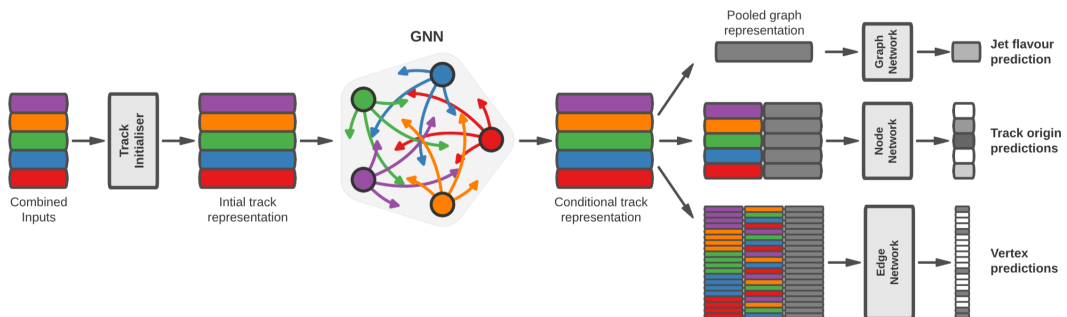


FIGURE 1.12: Schematic diagram of the GN1 model from Ref. [57].

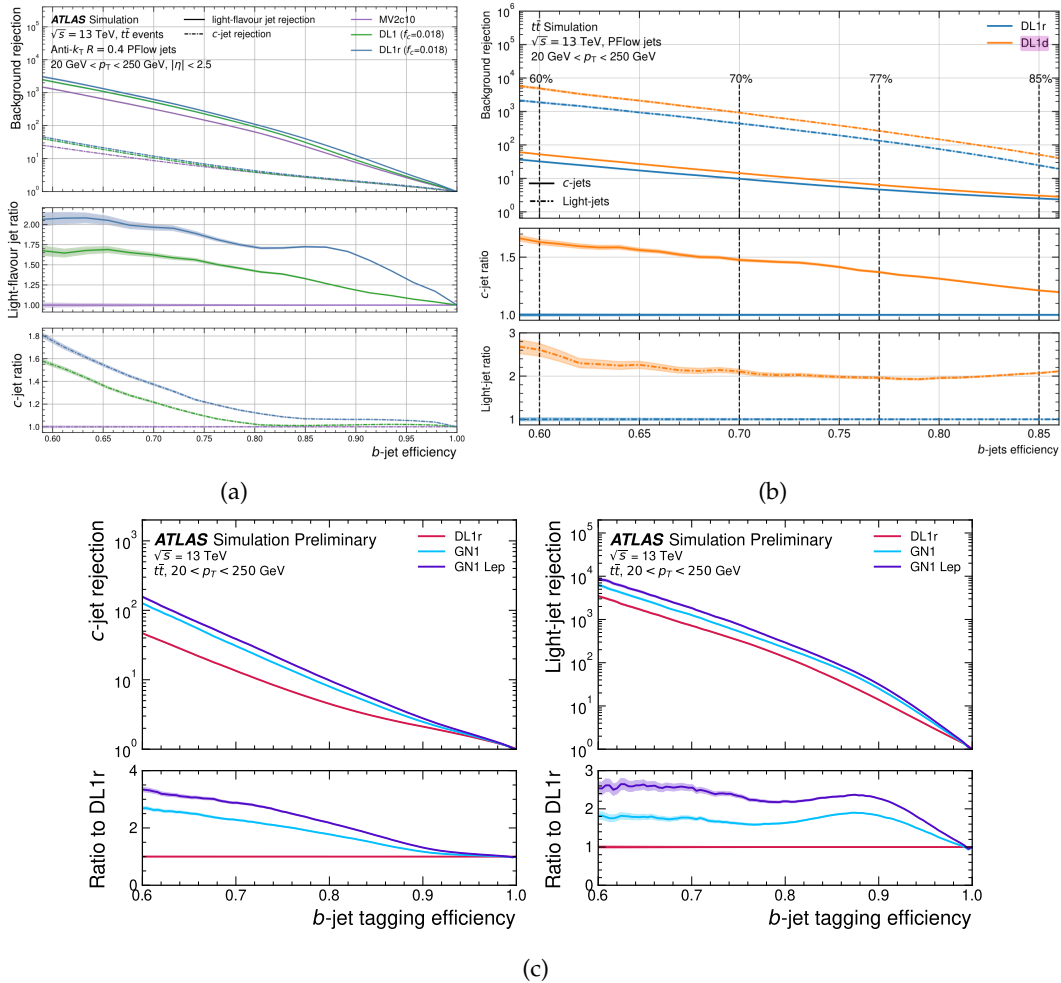


FIGURE 1.13: The rejection factors for light-jets and c-jets as a function of the b -tagging efficiency for the different algorithms used by ATLAS over the years as measured on simulated $t\bar{t}$ datasets. **(a)** shows the performance of the MV2, DL1, DL1r taggers with the bottom panels showing the performance ratio to MV2. **(b)** shows the performance of the DL1d and DL1r taggers with the bottom panels showing the performance ratio to DL1r. **(c)** shows the performance of the GN1 tagger. Images taken from Refs. [53, 56, 57] respectively.

Bibliography

- [1] O. S. Brüning et al. *LHC Design Report v1: The LHC Main Ring*. CERN Yellow Reports: Monographs. 2004.
DOI: [10.5170/CERN-2004-003-V-1](https://doi.org/10.5170/CERN-2004-003-V-1).
- [2] O. S. Brüning et al. *LHC Design Report v2: The LHC Infrastructure and General Services*. CERN Yellow Reports: Monographs. 2004.
DOI: [10.5170/CERN-2004-003-V-2](https://doi.org/10.5170/CERN-2004-003-V-2).
- [3] M. Benedikt et al. *LHC Design Report v3: The LHC Injector Chain*. CERN Yellow Reports: Monographs. 2004.
DOI: [10.5170/CERN-2004-003-V-3](https://doi.org/10.5170/CERN-2004-003-V-3).
- [4] L. Evans and P. Bryant. "LHC Machine". In: *Journal of Instrumentation* 3.08 (2008), S08001.
DOI: [10.1088/1748-0221/3/08/S08001](https://doi.org/10.1088/1748-0221/3/08/S08001).
- [5] ATLAS Collaboration. "The ATLAS Experiment at the CERN Large Hadron Collider". In: *Journal of Instrumentation* 3.08 (2008), S08003.
DOI: [10.1088/1748-0221/3/08/S08003](https://doi.org/10.1088/1748-0221/3/08/S08003).
- [6] CMS Collaboration. "The CMS Experiment at the CERN LHC". In: *Journal of Instrumentation* 3.08 (2008), S08004.
DOI: [10.1088/1748-0221/3/08/S08004](https://doi.org/10.1088/1748-0221/3/08/S08004).
- [7] LHCb Collaboration. "The LHCb Detector at the LHC". In: *Journal of Instrumentation* 3.08 (2008), S08005.
DOI: [10.1088/1748-0221/3/08/S08005](https://doi.org/10.1088/1748-0221/3/08/S08005).
- [8] ALICE Collaboration. "The ALICE Experiment at the CERN LHC". In: *Journal of Instrumentation* 3.08 (2008), S08002.
DOI: [10.1088/1748-0221/3/08/S08002](https://doi.org/10.1088/1748-0221/3/08/S08002).
- [9] LHCf Collaboration. "The LHCf Detector at the CERN Large Hadron Collider". In: *Journal of Instrumentation* 3.08 (2008), S08006.
DOI: [10.1088/1748-0221/3/08/S08006](https://doi.org/10.1088/1748-0221/3/08/S08006).
- [10] TOTEM Collaboration. "The TOTEM Experiment at the CERN Large Hadron Collider". In: *Journal of Instrumentation* 3.08 (2008), S08007.
DOI: [10.1088/1748-0221/3/08/S08007](https://doi.org/10.1088/1748-0221/3/08/S08007).
- [11] J. Pinfold et al. *Technical Design Report of the MoEDAL Experiment*. CERN-LHCC-2009-006, MoEDAL-TDR-001. 2009.
URL: <https://cds.cern.ch/record/1181486>.
- [12] FASER Collaboration. "The FASER Detector". In: *Journal of Instrumentation* 19.05 (2024), P05066.
DOI: [10.1088/1748-0221/19/05/P05066](https://doi.org/10.1088/1748-0221/19/05/P05066).
- [13] SND@LHC Collaboration. "SND@LHC: The Scattering and Neutrino Detector at the LHC". In: *Journal of Instrumentation* 19.05 (2024), P05067.
DOI: [10.1088/1748-0221/19/05/P05067](https://doi.org/10.1088/1748-0221/19/05/P05067).
- [14] F. Landua. "The CERN Accelerator Complex Layout in 2022. Complexe Des Accélérateurs Du CERN En Janvier 2022". In: (2022).
URL: <https://cds.cern.ch/record/2813716>.

- [15] ATLAS Collaboration. *Luminosity Public Results for Run-1*. 2024.
URL: <https://twiki.cern.ch/twiki/bin/view/AtlasPublic/LuminosityPublicResultsRun1>.
- [16] ATLAS Collaboration. *Public ATLAS Luminosity Results for Run-2 of the LHC*. 2024.
URL: <https://twiki.cern.ch/twiki/bin/view/AtlasPublic/LuminosityPublicResultsRun2>.
- [17] ATLAS Collaboration. *Public ATLAS Luminosity Results for Run-3 of the LHC*. 2024.
URL: <https://twiki.cern.ch/twiki/bin/view/AtlasPublic/LuminosityPublicResultsRun3>.
- [18] R. Bruce et al. "Review of LHC Run 2 Machine Configurations". In: (2019), pp. 187–197.
URL: <https://cds.cern.ch/record/2750415>.
- [19] S. Fartoukh et al. *LHC Configuration and Operational Scenario for Run 3*. CERN-ACC-2021-0007. CERN, 2021.
URL: <https://cds.cern.ch/record/2790409>.
- [20] ATLAS Collaboration. "The ATLAS Experiment at the CERN Large Hadron Collider: A Description Of The Detector Configuration For Run 3". In: *Journal of Instrumentation* 19.CERN-EP-2022-259 (05 2024), P05063.
DOI: [10.1088/1748-0221/19/05/P05063](https://doi.org/10.1088/1748-0221/19/05/P05063).
- [21] ATLAS tracking CP group. *ATLAS Tracking Software Tutorial*. 2024.
URL: <https://atlassoftwaredocs.web.cern.ch/internal-links/tracking-tutorial>.
- [22] M. Backhaus. "The Upgraded Pixel Detector of the ATLAS Experiment for Run 2 at the Large Hadron Collider". In: *Nuclear Instruments and Methods in Physics Research Section A: Accelerators, Spectrometers, Detectors and Associated Equipment*. Proceedings of the 10th International "Hiroshima" Symposium on the Development and Application of Semiconductor Tracking Detectors 831 (2016), pp. 65–70.
DOI: [10.1016/j.nima.2016.05.018](https://doi.org/10.1016/j.nima.2016.05.018).
- [23] ATLAS Collaboration. *Technical Design Report for the ATLAS Inner Tracker Pixel Detector*. CERN-LHCC-2017-021, ATLAS-TDR-030. CERN, 2017.
DOI: [10.17181/CERN.FOZZ.ZP3Q](https://doi.org/10.17181/CERN.FOZZ.ZP3Q).
- [24] ATLAS Collaboration. "Production and Integration of the ATLAS Insertable B-Layer". In: *Journal of Instrumentation* 13.05 (2018), T05008.
DOI: [10.1088/1748-0221/13/05/T05008](https://doi.org/10.1088/1748-0221/13/05/T05008).
- [25] ATLAS Collaboration. "Operation and Performance of the ATLAS Semiconductor Tracker". In: *Journal of Instrumentation* 9.08 (2014), P08009.
DOI: [10.1088/1748-0221/9/08/P08009](https://doi.org/10.1088/1748-0221/9/08/P08009).
- [26] B. Mindur. *ATLAS Transition Radiation Tracker (TRT): Straw Tubes for Tracking and Particle Identification at the Large Hadron Collider*. ATL-INDET-PROC-2016-001. CERN, 2017.
DOI: [10.1016/j.nima.2016.04.026](https://doi.org/10.1016/j.nima.2016.04.026).
- [27] ATLAS Collaboration. *ATLAS Liquid-Argon Calorimeter: Technical Design Report*. Technical Design Report. ATLAS. 1996.
DOI: [10.17181/CERN.FWRW.FOOQ](https://doi.org/10.17181/CERN.FWRW.FOOQ).
- [28] ATLAS Collaboration. *ATLAS Tile Calorimeter: Technical Design Report*. Technical Design Report. ATLAS. 1996.
DOI: [10.17181/CERN.JRBJ.7028](https://doi.org/10.17181/CERN.JRBJ.7028).

- [29] ATLAS Collaboration. *ATLAS Muon Spectrometer: Technical Design Report*. Technical Design Report. ATLAS. 1997.
URL: <https://cds.cern.ch/record/331068>.
- [30] ATLAS Collaboration. “Performance of the ATLAS Track Reconstruction Algorithms in Dense Environments in LHC Run 2”. In: *The European Physical Journal C* 77.10 (2017-10-11, 2017), p. 673.
DOI: [10.1140/epjc/s10052-017-5225-7](https://doi.org/10.1140/epjc/s10052-017-5225-7).
- [31] R. Frühwirth. “Application of Kalman Filtering to Track and Vertex Fitting”. In: *Nuclear Instruments and Methods in Physics Research Section A: Accelerators, Spectrometers, Detectors and Associated Equipment* 262.2 (1987), pp. 444–450.
DOI: [10.1016/0168-9002\(87\)90887-4](https://doi.org/10.1016/0168-9002(87)90887-4).
- [32] ATLAS Collaboration. “A Neural Network Clustering Algorithm for the ATLAS Silicon Pixel Detector”. In: *Journal of Instrumentation* 9.09 (2014), P09009.
DOI: [10.1088/1748-0221/9/09/P09009](https://doi.org/10.1088/1748-0221/9/09/P09009).
- [33] ATLAS Collaboration. “Reconstruction of Primary Vertices at the ATLAS Experiment in Run 1 Proton–Proton Collisions at the LHC”. In: *The European Physical Journal C* 77.5 (2017-05-19, 2017), p. 332.
DOI: [10.1140/epjc/s10052-017-4887-5](https://doi.org/10.1140/epjc/s10052-017-4887-5).
- [34] I. Sanderswood. *Development of ATLAS Primary Vertex Reconstruction for LHC Run 3*. 2019.
DOI: [10.48550/arXiv.1910.08405](https://doi.org/10.48550/arXiv.1910.08405).
- [35] G. Piacquadio and C. Weiser. “A New Inclusive Secondary Vertex Algorithm for B-Jet Tagging in ATLAS”. In: *Journal of Physics: Conference Series* 119.3 (2008), p. 032032.
DOI: [10.1088/1742-6596/119/3/032032](https://doi.org/10.1088/1742-6596/119/3/032032).
- [36] ATLAS Collaboration. *Secondary Vertex Finding for Jet Flavour Identification with the ATLAS Detector*. ATL-PHYS-PUB-2017-011. CERN, 2017.
URL: <https://cds.cern.ch/record/2270366>.
- [37] M. Cacciari, G. P. Salam, and G. Soyez. “The Anti- k_t Jet Clustering Algorithm”. In: *Journal of High Energy Physics* 2008.04 (2008), pp. 063–063.
DOI: [10.1088/1126-6708/2008/04/063](https://doi.org/10.1088/1126-6708/2008/04/063).
- [38] A. T. L. A. S. Collaboration. “Topological Cell Clustering in the ATLAS Calorimeters and Its Performance in LHC Run 1”. In: *The European Physical Journal C* 77.7 (2017-07-24, 2017), p. 490.
DOI: [10.1140/epjc/s10052-017-5004-5](https://doi.org/10.1140/epjc/s10052-017-5004-5).
- [39] A. Collaboration. *Variable radius, exclusive- k_T , and center-of-mass subjet reconstruction for higgs rightarrow $b\bar{b}$ tagging in ATLAS*. ATL-PHYS-PUB-2017-010. CERN, 2017.
URL: <https://cds.cern.ch/record/2268678>.
- [40] ATLAS Collaboration. “Jet Reconstruction and Performance Using Particle Flow with the ATLAS Detector”. In: *The European Physical Journal C* 77.7 (2017-07-13, 2017), p. 466.
DOI: [10.1140/epjc/s10052-017-5031-2](https://doi.org/10.1140/epjc/s10052-017-5031-2).
- [41] ATLAS Collaboration. *Tagging and Suppression of Pileup Jets with the ATLAS Detector*. ATLAS-CONF-2014-018. CERN, 2014.
URL: <https://cds.cern.ch/record/1700870>.
- [42] J. Thaler and K. Van Tilburg. “Identifying Boosted Objects with N-subjettiness”. In: *Journal of High Energy Physics* 2011.3 (2011), p. 15.
DOI: [10.1007/JHEP03\(2011\)015](https://doi.org/10.1007/JHEP03(2011)015).

- [43] C. Hackstein and M. Spannowsky. "Boosting Higgs Boson Discovery: The Forgotten Channel". In: *Physical Review D* 82.11 (2010), p. 113012.
DOI: [10.1103/PhysRevD.82.113012](https://doi.org/10.1103/PhysRevD.82.113012).
- [44] A. J. Larkoski, G. P. Salam, and J. Thaler. "Energy Correlation Functions for Jet Substructure". In: *Journal of High Energy Physics* 2013.6 (2013), p. 108.
DOI: [10.1007/JHEP06\(2013\)108](https://doi.org/10.1007/JHEP06(2013)108).
- [45] A. J. Larkoski, I. Moult, and D. Neill. "Power Counting to Better Jet Observables". In: *Journal of High Energy Physics* 2014.12 (2014), p. 9.
DOI: [10.1007/JHEP12\(2014\)009](https://doi.org/10.1007/JHEP12(2014)009).
- [46] P. T. Komiske, E. M. Metodiev, and J. Thaler. "Energy Flow Polynomials: A Complete Linear Basis for Jet Substructure". In: *Journal of High Energy Physics* 2018.4 (2018), p. 13.
DOI: [10.1007/JHEP04\(2018\)013](https://doi.org/10.1007/JHEP04(2018)013).
- [47] A. T. L. A. S. Collaboration. "Configuration and Performance of the ATLAS B-Jet Triggers in Run 2". In: *The European Physical Journal C* 81.12 (2021-12-09, 2021), p. 1087.
DOI: [10.1140/epjc/s10052-021-09775-5](https://doi.org/10.1140/epjc/s10052-021-09775-5).
- [48] ATLAS Collaboration. "ATLAS B-Jet Identification Performance and Efficiency Measurement with $t\bar{t}$ Events in Pp Collisions at $\sqrt{s}=13$ TeV". In: *The European Physical Journal C* 79.11 (2019-11-25, 2019), p. 970.
DOI: [10.1140/epjc/s10052-019-7450-8](https://doi.org/10.1140/epjc/s10052-019-7450-8).
- [49] ATLAS Collaboration. *Calibration of the Performance of b-Tagging for c and Light-Flavour Jets in the 2012 ATLAS Data*. ATLAS-CONF-2014-046. CERN, 2014.
URL: <https://cds.cern.ch/record/1741020>.
- [50] ATLAS Collaboration. *Expected Performance of the ATLAS b-Tagging Algorithms in Run-2*. ATL-PHYS-PUB-2015-022. CERN, 2015.
URL: <https://cds.cern.ch/record/2037697>.
- [51] A. Collaboration. *Optimisation and performance studies of the ATLAS b-tagging algorithms for the 2017-18 LHC run*. ATL-PHYS-PUB-2017-013. CERN, 2017.
URL: <https://cds.cern.ch/record/2273281>.
- [52] ATLAS Collaboration. *Identification of Jets Containing b-Hadrons with Recurrent Neural Networks at the ATLAS Experiment*. ATL-PHYS-PUB-2017-003. CERN, 2017.
URL: <https://cds.cern.ch/record/2255226>.
- [53] ATLAS Collaboration. "ATLAS Flavour-Tagging Algorithms for the LHC Run 2 Pp Collision Dataset". In: *The European Physical Journal C* 83.7 (2023), p. 681.
DOI: [10.1140/epjc/s10052-023-11699-1](https://doi.org/10.1140/epjc/s10052-023-11699-1).
- [54] ATLAS Collaboration. *Deep Sets Based Neural Networks for Impact Parameter Flavour Tagging in ATLAS*. ATL-PHYS-PUB-2020-014. CERN, 2020.
URL: <https://cds.cern.ch/record/2718948>.
- [55] M. Zaheer et al. "Deep Sets". In: *Advances in Neural Information Processing Systems*. Vol. 30. 2017.
DOI: [10.48550/arXiv.1703.06114](https://doi.org/10.48550/arXiv.1703.06114).
- [56] A. Froch. "Heavy-flavour tagging and measurement of the $t\bar{t}H$ production cross-section in the $H \rightarrow b\bar{b}$ decay channel at the ATLAS Experiment". Albert-Ludwigs-Universität Freiburg, 2024.
DOI: [10.6094/UNIFR/258524](https://doi.org/10.6094/UNIFR/258524).
- [57] ATLAS Collaboration. *Graph Neural Network Jet Flavour Tagging with the ATLAS Detector*. ATL-PHYS-PUB-2022-027. CERN, 2022.
URL: <https://cds.cern.ch/record/2811135>.